

Representation of dry tropical layers and their origins in ERA-40 data

Piero Cau, John Methven, and Brian Hoskins

Department of Meteorology, University of Reading, Reading, UK

Received 19 April 2004; revised 4 November 2004; accepted 18 January 2005; published 22 March 2005.

[1] The focus of this paper is the occurrence of dry intrusions in the tropical atmosphere and their origin. Dry layers are observed to have a wide range of thicknesses, so as guidance on the scales of interest the radiative impact of dry intrusions is investigated. Typically such intrusions would contribute an increase in OLR of 3 Wm^{-2} per 100 hPa thickness in a clear-sky scenario and less if clouds are present. The velocity fields from ERA-40 are used to calculate the back trajectories of air masses from radiosonde profiles. The humidity observed by the sondes is compared with humidity profiles reconstructed by taking ERA-40 specific humidity from the origin of the trajectories, reducing the value only if saturation occurs along the trajectory. The agreement found provides a validation of the trajectory technique used, which is then used to infer the origin of dry air masses during November and December 1992 at Kapingamarangi, in the tropical West Pacific. A variety of behaviors is found, with many dry events clearly associated with air masses descending from the extratropics. Four particular dry events are discussed.

Citation: Cau, P., J. Methven, and B. Hoskins (2005), Representation of dry tropical layers and their origins in ERA-40 data, *J. Geophys. Res.*, 110, D06110, doi:10.1029/2004JD004928.

1. Introduction

[2] The occurrence of dry intrusions in the tropics has been extensively studied during the intensive observing period of TOGA-COARE, the Coupled Ocean-Atmosphere Response Experiment of the Tropical Ocean and Global Atmosphere project [Webster and Lukas, 1992]. Pierrehumbert [1995] has shown that the dryness of the tropospheric air in the subtropics and some regions in the tropics is important because it has a strong influence on the ability of the climate system to radiate heat to space and on the prevention of a runaway greenhouse effect. In addition, dry intrusions are known to be dynamically active. Mapes and Zuidema [1996] show that dry intrusions obtained from a composite of TOGA COARE data are characterized by extremely high moisture gradients and corresponding positive temperature gradients at their lower edge. They show how the long-wave radiation results in anomalous heating in the dry air above an anomalous cooling in the underlying moist air, thus stabilizing the bottom of the dry intrusion. The temperature inversion and humidity drop can often be sufficiently strong to cap convection, preventing its penetration into the higher troposphere. Investigating the origin of dry air masses in their detailed analysis of the intensive observing period of the TOGA-COARE program, Yoneyama and Parsons [1999] have shown that most observed dry intrusions into the tropical lower troposphere are associated with advection of air directly from the subtropics and even extratropics. In addition, Mapes and Zuidema [1996] have shown that the dry tongues observed over the tropical West Pacific, although

associated with a warm anomaly, are far too dry to have resulted from an adiabatic displacement within the tropics. They argued that the descent of the dry air must take place over 5 days or so during which time there is substantial radiative cooling.

[3] In this paper the origin of dry intrusions as inferred using the ECMWF 40-year Re-Analysis (ERA-40) data set [Simmons and Gibson, 2000] is studied. This data set has a high temporal and spatial resolution, with a grid-spacing close to 125 km in the horizontal and with sixty levels in the vertical located between the surface and a height of about 65 km. The analyses are provided every 6 hours throughout the period from mid-1957 to 2001, and take advantage of 3D-VAR data-assimilation techniques.

[4] In section 3, as a guidance for the rest of the study on which dry intrusions may be of importance, their radiative impact is investigated including the effects of cloud layers above and below. The focus is on the dependence of radiative transfer on the altitude and thickness of such intrusions. In section 4 the analyzed humidity from ERA-40 is then compared with radiosonde data from Kapingamarangi, one of the stations involved in the TOGA-COARE experiment and the closest one to the equator. The representation of dry events is shown and also compared with results from the earlier ERA-15 [Gibson *et al.*, 1997]. In section 5.1, back trajectories are then used to infer the origin of air masses in the tropics and investigate the accuracy of this technique. Previously trajectory accuracy has only been analyzed in detail for the extratropics [e.g., Stohl, 1998; Methven *et al.*, 2003]. The dependence of correlation between the observed and reconstructed humidity profiles on trajectory length, with varying degrees of smoothing in the vertical is discussed.

In section 6, back trajectories that match low humidity events in the observations at Kapingamarangi are shown to illustrate a variety of interesting behavior.

2. Method

[5] A subset of radiosonde observations collected during the intensive observation period of the TOGA COARE project (November 1992 to February 1993) is studied. This subset consists of 161 soundings from Kapingamarangi ($154^{\circ}48.00'E$, $01^{\circ}04.33'N$), covering all of November and December 1992 with the exception of those flights whose records contain a negative/unclear comment from the operator. All observational data include the corrections discussed by Wang *et al.* [2002] and Ciesielski and Johnson [2003]. The relative humidity is quoted with respect to water (RH_w), but throughout this paper it has been converted to RH with respect to water and ice (RH_{wi}). This is done by first converting RH_w to specific humidity following Nordquist [1973] and then to RH_{wi} following Simmons *et al.* [1999]. The saturation vapor pressure used in this last conversion is that over water for temperatures above $0^{\circ}C$ and that over ice for temperatures below $-23^{\circ}C$. Between these two limits, a quadratic fit in temperature is used.

[6] The radiative calculations presented in section 3 use a narrow-band radiative transfer scheme which includes both short wave (SW) and long wave (LW) radiation, as implemented in a code developed by K. Shine and collaborators [Shine, 1991]. In all the calculations both CO_2 and O_3 are included, and an albedo for the ground of 0.3 is adopted. Given a fixed temperature profile, the transfer of radiation is calculated in the spectral region $0-3000\text{ cm}^{-1}$. The atmospheric column is divided into 92 layers (of which only 3 are above 100 hPa), and the transfer of SW and LW radiation is modelled for a number of times during the day and then averaged. Incoming solar (SW) radiation is appropriate for the location and period of the year of the observations considered in this paper.

[7] We use back trajectories in order to “reconstruct” the vertical humidity profile and thus identify the dry regions with their origin. If this identification is positive, we can use the trajectories to infer the origin of the dry air. The back trajectories are calculated by the U.K. Universities Global Atmospheric Modelling Programme (UGAMP) offline trajectory model [Methven, 1997] by integrating velocity with respect to time using a 4th order Runge-Kutta scheme. The term “offline” indicates that the dynamical equations of the atmosphere are not integrated as part of the trajectory model. Fields (e.g., velocity, temperature, humidity) at particle positions are obtained from the ECMWF analyses by cubic Lagrange interpolation in the vertical followed by bilinear interpolation in the horizontal and linear interpolation in time. The details can be found in Methven [1997] together with estimates of the errors in trajectories arising from the interpolation of discretized wind fields.

[8] For each record of humidity in the soundings, a trajectory is “released” from the corresponding position and time. Specific humidity is interpolated in space and time from the analysis to the origin of each back trajectory τ days in the past and assigned to the trajectory, $q_{traj} = q(t_0 - \tau)$. In the absence of mixing or water phase changes, specific humidity would be conserved, such that $q(t_0) = q(t_0 - \tau)$.

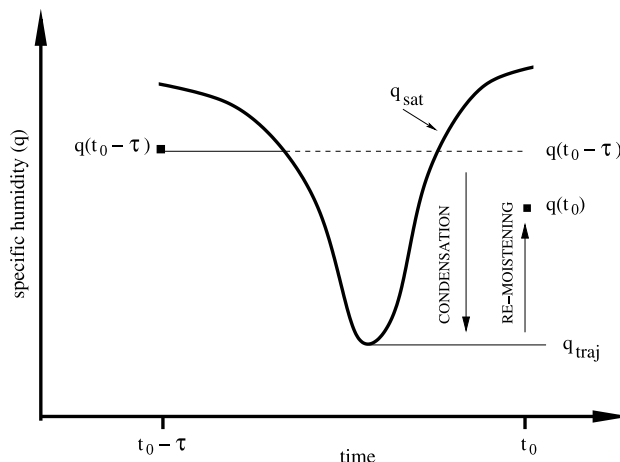


Figure 1. The assignment of specific humidity, q , to a back trajectory. Assuming no mixing or condensation, q is conserved along the trajectory. If trajectories of τ days are considered, the value $q(t_0 - \tau)$ of specific humidity analyzed at their origin is assigned to them. If along the trajectory $q(t_0 - \tau)$ is higher than the saturation point, the lowest value of the saturation specific humidity along the trajectory ($\min(q_{sat})$) is assigned to it (q_{traj}). The difference between $q(t_0 - \tau)$ and q_{traj} is an indication of condensation occurring along the trajectory. The difference between $q(t_0)$ (the specific humidity from the analysis at the arrival point of the trajectory) and q_{traj} is an indication of all other processes affecting humidity since saturation last occurred.

[9] However, as illustrated in Figure 1, we also compute the lowest value of the saturation specific humidity, $\min(q_{sat})$, along the trajectory. If $\min(q_{sat}) < q(t_0 - \tau)$ (i.e., if condensation must have occurred along the trajectory), we assign $\min(q_{sat})$ to the trajectory instead of $q(t_0 - \tau)$. No moistening processes are considered in this simple model. q_{traj} is transformed into RH_{wi} following Simmons *et al.* [1999] (see above) to calculate the saturation vapor pressure and then using the standard formula with temperature and pressure from the analysis at time t_0 .

[10] Radiosonde humidity profiles contain a large amount of small-scale detail (typically a profile in our data set contains 500–700 records of relative humidity) that, as discussed in section 3, are almost irrelevant in their radiative impact and would be impossible to reproduce exactly using back trajectories. For this reason both the RH profiles determined by our model and those measured by the radiosondes are also smoothed. This is done using a Savitzky-Golay filter [Press *et al.*, 1992], which is defined as weighted moving average with weighting given as a polynomial of a certain degree (2nd in our case, chosen after various tests). The coefficients are those of a polynomial least-square fit within the filter window. This polynomial is designed to preserve higher moments within the data and reduce the bias introduced by the filter, thus allowing us to preserve the position and width of dry intrusions. Since the filter requires the values to be distributed on a regular grid, before smoothing we interpolate the radiosonde data and the model results onto a regular grid (starting at 1000 hPa and decreasing to 100 hPa with grid spacing of 1 hPa). The width of the filter is decided on the basis of the results of

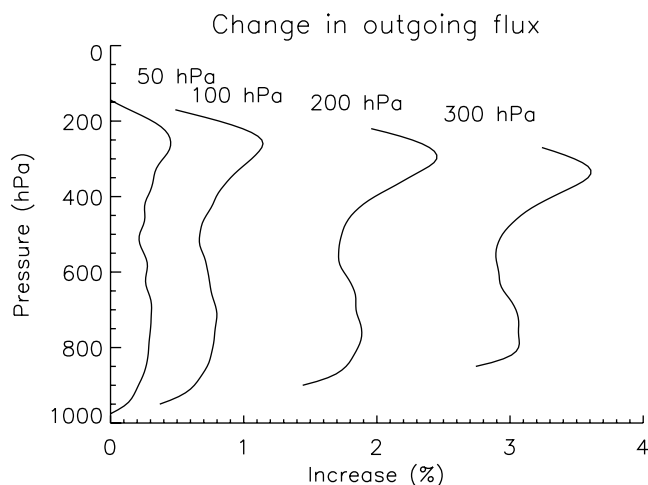


Figure 2. Percentage increase in OLR from the top of the atmosphere when a moving dry window of 50 hPa, 100 hPa, 200 hPa and 300 hPa replaces part of the mean observed RH profile given in Figure 9. The moving dry windows are defined by having RH = 20% and the y-axis shows their central pressure.

section 3 which show that in a clear sky scenario a 100 hPa thick dry intrusion contributes a 3 Wm^{-2} increase in outgoing longwave radiative flux. This leads us to concentrate our study on dry intrusions of 50 hPa or thicker, and accordingly we choose filter widths of 50 hPa or 100 hPa. Incidentally, the use of such widths produces profiles of humidity whose level of detail is comparable with that of ERA-40 analyses. The reconstructed specific humidity, q_{traj} , is richer in detail, but the relative humidity is calculated from it using temperature and pressure profiles at the time of observation, the resolution of which is that of the analysis.

[11] The agreement between the RH humidity profile from a radiosonde (above 800 hPa) and that reconstructed by the trajectory model was determined using the Pearson's correlation coefficient between the two when their time-average profiles have been removed, i.e., between their anomalies (see section 5.2 and Figure 10). The correlation is not studied below 800 hPa because of significant moistening occurring there; a process that is not included in our model. To evaluate the significance of the correlation, given that both the observed and reconstructed profiles show some auto-correlation, we estimate a confidence interval for the correlation using the bootstrap approach for serially dependent series described in *Mudelsee* [2003] and *Politis and Romano* [1994].

3. Radiative Effect of Dry Intrusions

[12] The motivation for the calculations presented in this section is to provide guidance for the intensity and vertical extent of dry intrusions whose behavior should be assessed in the back trajectory analysis. Here we present three sets of results. The first one corresponds to a clear sky radiative calculation when the humidity profile averaged over our sample is used, and a moving dry intrusion is added to the profile. This dry intrusion is defined as having a relative humidity of 20%. The second and third sets consider real cases, i.e., four different dry events taken from our data set.

The second set considers the dry intrusion assuming a clear sky scenario, while the third set also includes cloud layers.

3.1. Clear-Sky Scenario

[13] The first set of results is obtained using the mean humidity profile from our sample, which is described in section 4 (see Figure 9, thick line). We have used this humidity profile to model the radiative transfer in a column of atmosphere whose other parameters are those typical for the tropics. The fluxes at the top of the atmosphere for the mean vertical profile are 280.6 Wm^{-2} in the LW and 317.0 Wm^{-2} in the SW.

[14] We focus on the LW radiation and investigate how the outgoing flux given above is affected by dry intrusions of different width and at different heights. A moving layer of given width (50 hPa, 100 hPa, 200 hPa and 300 hPa) is removed from the mean humidity profile and replaced with a dry intrusion defined as having a relative humidity (RH) of 20%. Calculations are performed independently for each width, at each height.

[15] Figure 2 shows the percentage increase in the outgoing LW radiative (OLR) flux at the top of the atmosphere which occurs when the dry intrusion is introduced. The value plotted at a given pressure corresponds to the outgoing flux obtained when the layer of dry air was centered at that given pressure. A comparison of the outgoing flux with the width of the dry intrusion shows that the relation between the two is roughly linear. Fitting a linear relation, the increase in flux due to the occurrence of a dry intrusion (RH = 20%) is about 3 Wm^{-2} per 100 hPa thickness.

[16] Note that these idealized results depend on the way we have defined a dry intrusion. Figure 9 shows that the RH profile changes significantly with height, so replacing part of it with a layer of 20% affects the specific humidity by different amounts at different heights. Also the impact of upper tropospheric absolute humidity changes is larger due to more LW radiating directly to space, as shown explicitly by *Shine and Sinha* [1991].

3.2. Observed Dry Intrusions

[17] We have performed the same radiative calculation using four cases with dry intrusions from the radiosonde data set, all depicted in the first column of Figure 3 which shows the vertical profile of relative humidity. In order to isolate the effect of the dry intrusion on radiative transfer, similar calculations are performed with each profile, but replacing the dry intrusion with a linear fitting in RH between its edges, as shown in Figure 3.

[18] Figure 4 shows the increase in OLR due to the presence of a dry intrusion per 100 hPa thickness. The position on the y-axis corresponds to the central pressure of each intrusion. In all cases the OLR increases by about 3 Wm^{-2} per 100 hPa thickness as found for idealized dry layers in section 3.1. The impact of a dry intrusion is smaller when it lies close to the ground.

3.3. Cloud Scenarios

[19] The radiative transfer calculations, with and without the dry intrusion, are repeated assuming the presence of cloud decks at specified heights. Our clouds are defined by assuming that the liquid water in the column is concentrated into a single model layer and we use the liquid water

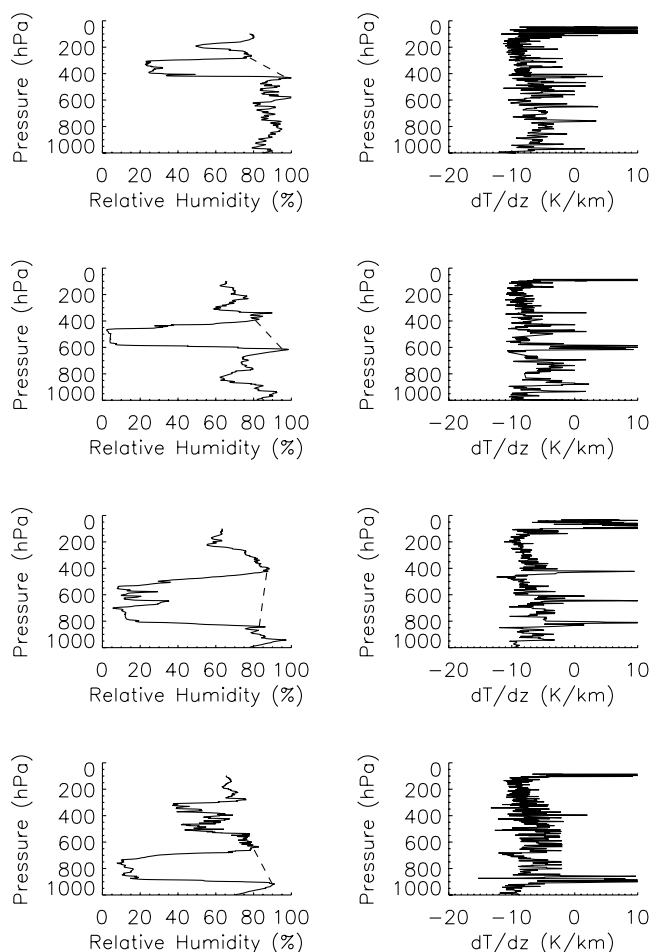


Figure 3. Relative humidity (with respect to liquid water, as recorded by the rawinsonde and after the corrections discussed by Wang *et al.* [2002] and Ciesielski and Johnson [2003]) and lapse rate profiles for four different dry events as given by TOGA COARE observations at Kapingamarangi. The linear fitting used to replace the dry intrusions is also shown (dashed lines). On the right, temperature inversions can be observed at the edges of dry intrusions, particularly in the lower troposphere. From top to bottom, their sonde index and date are 33 (10 November 1992, 17:00), 143 (22 December 1992, 17:03), 160 (30 December 1992, 11:05) and 38 (13 November 1992, 11:00).

column amount of 57 gm^{-2} . Two different cases are considered: (1) when the cloud is just on top of the dry intrusion (diamonds in Figure 4), and (2) when the cloud is at the lower edge of the intrusion (triangles).

[20] The radiative impact of a dry intrusion on the outgoing LW flux is reduced very significantly (to few tenths of Wm^{-2}) when a cloud lies above it. Similar results are obtained when the cloud is not close to the dry intrusion but occurs in the upper troposphere. The cloud has less influence on the impact of the dry intrusion on the outgoing radiation when it occurs below the dry intrusion (triangles). This situation occurs at various times in the data set used in this paper, and it is important to consider it because the cooling from the cloud layer acts to increase the stability at the bottom of the intrusion, helping to cap convection from

below, and therefore maintaining the dry layers. The importance of this effect was probably recognized for the first time by Namias [1936], who showed from observations that when dry air overlies moist, the interface tends to be anomalously stable.

[21] The four dry intrusions we have already considered (Figure 3) are appropriate for this investigation, because in all of them a significant dry intrusion lies above air which is close to saturation. Also, they occur at different heights, so we can investigate how the height at which the dry intrusion occurs can change the picture. The second column in Figure 3 shows the temperature lapse rate calculated by centered finite difference from the radiosonde temperature profile. Corresponding to the lower edges of the dry intrusion, temperature inversions can be observed in the form of positive spikes.

3.4. Radiative Heating

[22] The dry intrusion itself has a role in affecting the radiative heating rate. To investigate this point we calculate the difference in the net heating rates obtained when the dry intrusion is considered and when it is removed. This calculation is performed both in the clear-sky scenario and when a cloud is present at the lower edge of the intrusion. Results are shown in Figure 5, in which the thick and thin lines correspond respectively to the clear-sky and the lower-cloud scenarios. In all cases, the dry intrusion intensifies the cooling below its lower edge since the dry intrusion is more transparent to upward LW. The cooling rate decreases (positive in Figure 5) within the dry intrusion because there is less water radiating and also decreases above the intrusion since there is more absorption by the unperturbed water

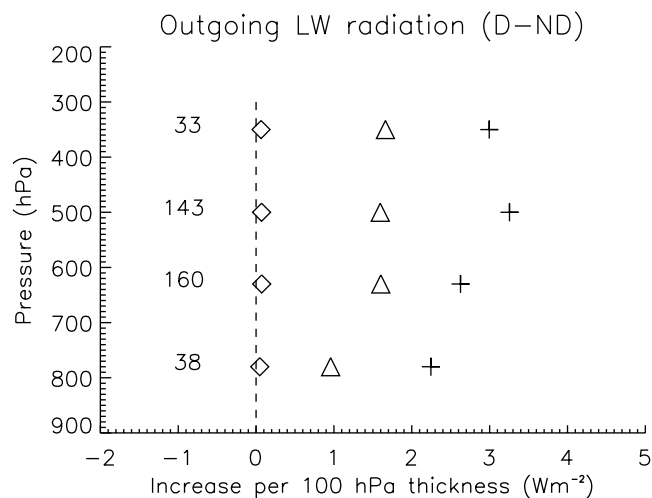


Figure 4. Increase in the outgoing LW flux (Wm^{-2}) induced by the presence of the dry intrusions shown in Figure 3, normalized by their thickness, shown for three different cases: clear sky (crosses) and when a cloud is present at the lower edge (triangles) or upper edge (diamonds) of the dry intrusion. The y-axis shows the central pressure of each of the four intrusions, and the value on the x-axis is the increase in the flux per 100 hPa thickness when the dry intrusion is considered (D) minus the flux obtained when the dry intrusion is replaced by a linear fitting between its edges (ND), as shown in Figure 3.

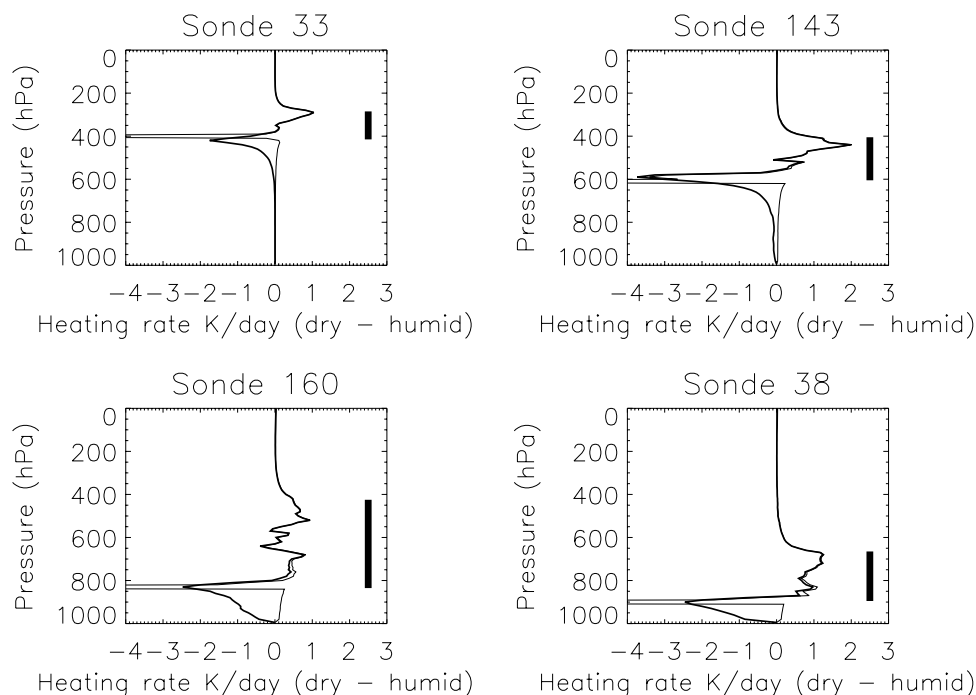


Figure 5. Difference between the net radiative heating rate (K/day) obtained for the dry intrusions considered in Figure 3 and that obtained when the dry intrusion is replaced with a linear fitting between its edges, as shown in Figure 3. The position of the dry intrusion is shown by the vertical bar on the right in each plot. Positive differences correspond to a less efficient cooling when the dry intrusion is considered. The thick line corresponds to the clear-sky scenario, while the thin one corresponds to the case in which a cloud is present at the lower edge of the intrusion. In both scenarios a cooling occurs just below the dry layer. The minima in the case of a cloud is as low as -30 K/day for sonde 38.

vapor there. In other words, irrespective of the presence of clouds, the dry intrusion is able to affect the temperature lapse rate. Although the insertion of a cloud layer into the model concentrates the cooling below the dry intrusion onto the cloud top level, the net effect on the top of atmosphere LW flux is actually greater in the clear-sky case (compare crosses and triangles in Figure 4).

4. Consistency of Analysis With Observations

[23] Figure 6 shows the percentiles of the distribution of relative humidity (RH_{wi}) in the radiosonde data set. It is clear that dry air masses with $RH_{wi} < 20\%$ occur more than 10% of the time in the mid to upper troposphere but less than 10% of the time below 600 hPa.

[24] This investigation also gives the opportunity to investigate the agreement between ERA-15 [Gibson *et al.*, 1997] and ERA-40 [Simmons and Gibson, 2000] humidity fields by comparing them with observed humidity profiles from radiosondes. An immediate comparison is offered in Figure 7. Here the relative humidity profiles of all sondes in the sample are shown in the top plot. Each vertical line is a humidity profile corresponding to a certain sonde, identified with its index on the x-axis. The correspondence between this index and the date at which the sounding occurred is given in Figure 8. The occurrence of dry intrusions can be seen in the form of dark-blue patches. The other two plots are the same but derived from the analysis of ERA-40 (middle plot) and that of ERA-15 (bottom). Both analyses capture the dry events but ERA-15 has a dry bias in the

upper troposphere. The TOGA-COARE sondes were assimilated into both reanalyses and so the better RH in ERA-40, also shown in section 5.1, must arise through improvements in the ECMWF forecast model and data assimilation system. The main changes [Simmons, 2001] that are likely to have affected the relative humidity are: (1) better data assimila-

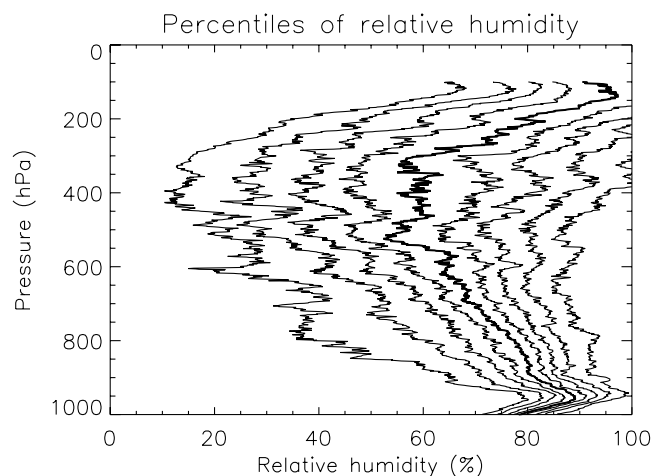


Figure 6. Percentiles of the cumulative distribution of relative humidity (with respect to water and ice) in the sample of 161 soundings from the TOGA COARE project. The thick line in the center corresponds to the median RH and all the lines are separated by 10%, from 10% to 90%.

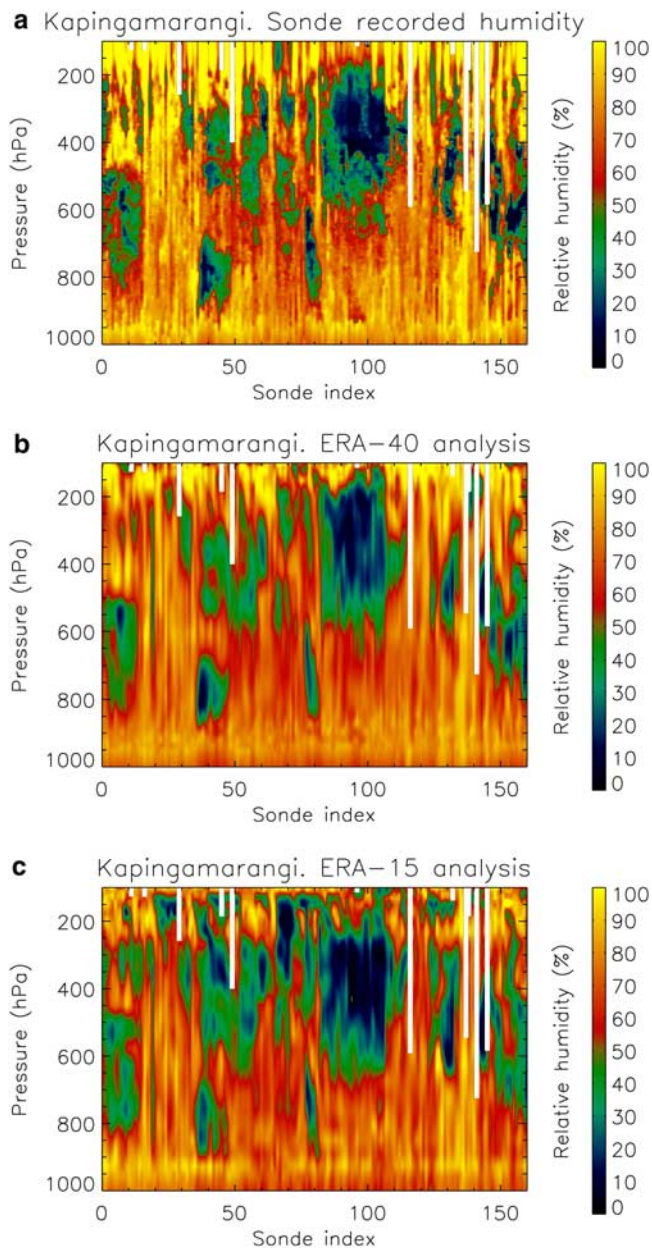


Figure 7. Profile of relative humidity (recalculated with respect to water and ice, see section 2) for all sondes included in our sample from Kapingamarangi. The x-axis labels consecutive soundings, and the correspondence between index and date is given in Figure 8. The lower two panels show the RH from ERA-40 and ERA-15 interpolated in space and time to the sonde position.

tion scheme with the replacement of Optimal Interpolation by 3D-Var together with the inclusion of more satellite data including SSM/I humidity and TOVS radiance data; (2) major changes in the parametrization of deep convection, clouds and vertical diffusion; (3) improvements to the Semi-Lagrangian advection scheme; (4) better resolution in the vertical in both the boundary layer and the stratosphere, almost doubling the number of levels from 31 to 60 (horizontal resolution was not changed); (5) more accurate calculation of saturation vapor pressure for cold temper-

atures [Simmons *et al.*, 1999]. The average humidity profiles from ERA-15 and ERA-40 are investigated in section 5.1.

5. Comparison of Trajectory Model With Observations

5.1. Average Profiles From the Trajectory Model

[25] The profiles of RH for all sondes in our data set are reconstructed using trajectories driven by ERA-15 and ERA-40 winds, and their average profiles are shown in Figure 9. It can be seen that the reconstructed humidity (thin lines) is typically drier than the observations (thick line) using both ERA-15 and ERA-40, though ERA-40 shows a much closer agreement with the observations above 600 hPa. Given its much better agreement with observation, all results presented in the rest of this paper are obtained using ERA-40 fields and we will not make any further use of the earlier ERA-15 analysis.

[26] As trajectory length increases the reconstructed profile becomes drier because moistening processes are not modelled. Moistening is most rapid in the boundary layer over the Pacific Ocean and above this is most likely associated with convection. Interestingly, the trajectory model indicates that if moistening did not occur, within a week the RH profile would become almost uniform with height below 300 hPa.

[27] The average profile of relative humidity can be compared with Figure 2 of Ciesielski and Johnson [2003]. They show an average relative humidity profile from all stations where Vaisala-H humidity sensors were used (including Kapingamarangi). The comparison shows a very good agreement up to about 200 hPa. Above it, their profile is drier (by about 10%), because Kapingamarangi is close to the equator, where the upper tropospheric humidity is higher (see their Figure 8).

5.2. Correlation and Its Preservation Along Trajectories

[28] To estimate the agreement between the observed profile and those reconstructed using trajectories of different lengths, we first subtract their time average profiles and then estimate the Pearson coefficient (r) between them using a bootstrap approach (see section 2). We are interested in cases with good correlation, and choose to test the hypothesis that $r > 0.5$ at the 50% and 95% significance level. Figure 10 shows, for varying trajectory lengths, the percentage of reconstructed profiles which have a correlation significantly higher than 0.5 at the confidence levels of 50% and 95%. The results are shown for the nonsmoothed profiles and for the smoothed profiles using filter widths of 50 hPa and 100 hPa. Trajectories of length 0 correspond to the reanalysis. The use of a trajectory model over a 6 hour window actually improves the representation of humidity profiles. However, the correlation then decreases rapidly out to 1 day. Beyond 1 day, the correlation with the trajectory model persists or falls slowly.

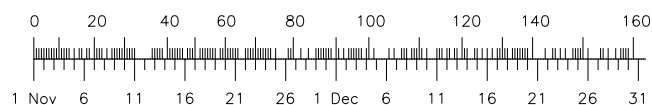


Figure 8. Correspondence between sonde index and launch date.

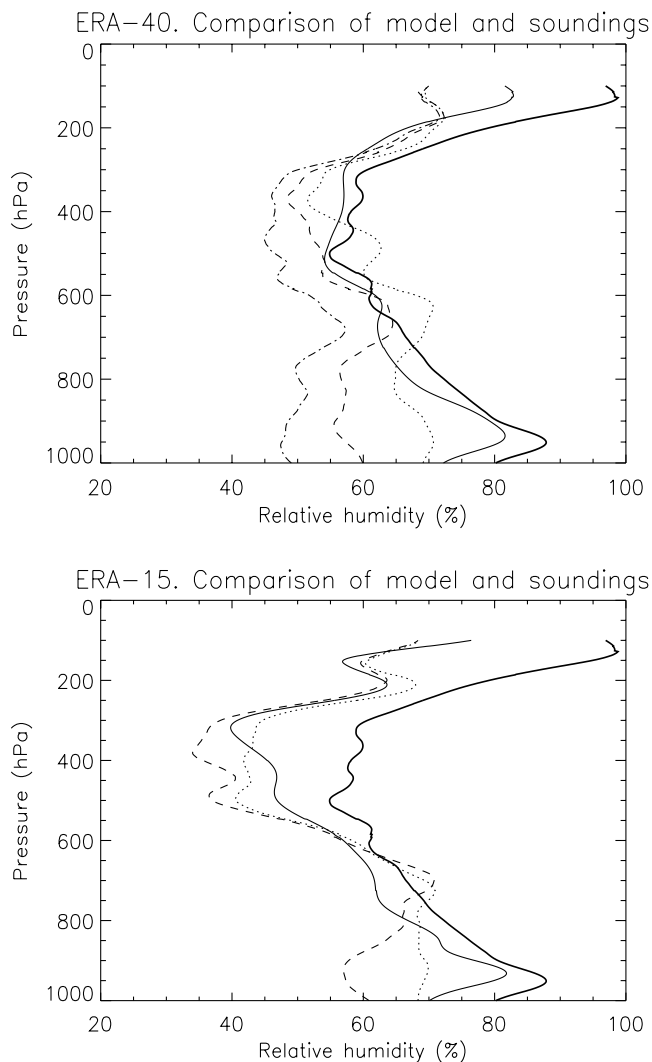


Figure 9. Time-averaged relative humidity profiles of the soundings (thick line) and those reconstructed using ERA-40 data (top) and ERA-15 data (bottom). The thin continuous line corresponds to the analysis, and the other thin lines correspond to the humidity profiles reconstructed using back trajectories with a length of 3 (dotted), 5 (dashed) and 7 (dot-dashed) days (7 days shown for ERA-40 only).

Smoothing in the vertical clearly improves the correlation, but does not significantly affect the decay with increasing trajectory length. More than half the profiles reconstructed using 7-day back trajectories and a 50 hPa vertical filter have a correlation with radiosonde observations greater than 0.5 at the 50% confidence level (in other words the median estimate of their correlation exceeds 0.5).

5.3. Agreement Over Moving Windows

[29] The most common error in the trajectory model representation of a profile is that dry layers exist and match those observed but that they have small displacement errors. The correlation investigated in the previous section penalizes those cases with strong intrusions that have displacement errors similar to their depth.

[30] In this section we investigate the occurrence of agreements over moving windows of various widths, agree-

ment being defined as the occurrence of a dry intrusion (i.e., relative humidity < 20%) in both the model and the radiosonde data at any point within the window.

[31] Figure 11 shows the agreement over a 100 hPa window when trajectories of (a) 3 days and (b) 7 days are used. A grey point marks the center of a window over which the trajectory model predicts the presence of at least one dry intrusion. When this prediction is confirmed by the soundings, i.e., if both the radiosonde and the model predict a dry intrusion anywhere on the same window, the center of that window is shown as a black pixel in the plot. Comparison with Figure 7 (top) shows that almost all intrusions are picked up by the model using trajectories of 3 days. Longer trajectories result in more dry points in the model, but they are clustered around the same events observed by the sondes.

[32] Figures 11c and 11d show the result for moving windows of 50 hPa and 150 hPa obtained when using trajectories of 7 days. The dry events appear as clusters in these plots. The important result here is that the 50 hPa window results contain the same events as in those for the 150 hPa windows, though of course there are more “agreements” within wider layers.

[33] The results of Figure 11 can be compared with Figure 3b of *Yoneyama and Parsons [1999]*, though they use a different definition for dry events based on departure from the mean humidity by more than one or two standard deviations. There is quite good agreement, providing evidence that our definition of dryness based on a constant threshold in RH is consistent with an approach based on the statistics of specific humidity.

6. Origin of Dry Air Masses

6.1. General Discussion

[34] Figure 12a shows the change in pressure along trajectories during 7 days following the flow resolved in ERA-40. A negative value of the change in pressure denotes air which

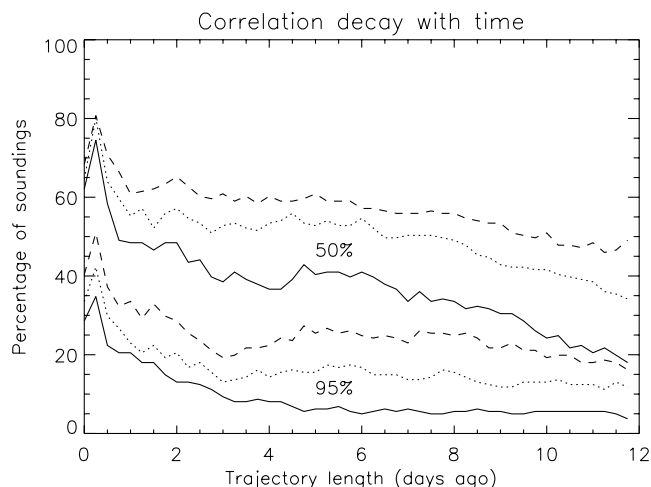


Figure 10. Time evolution of the percentage of the 161 soundings having a correlation significantly larger than 0.5 at the confidence levels of 95% (three lower lines) and 50% (three upper lines). In each case, the three lines correspond to the unsmoothed RH profiles (solid line), and profiles smoothed with a Savitzky-Golay filter of width 50 hPa (dotted line) and 100 hPa (dashed line).

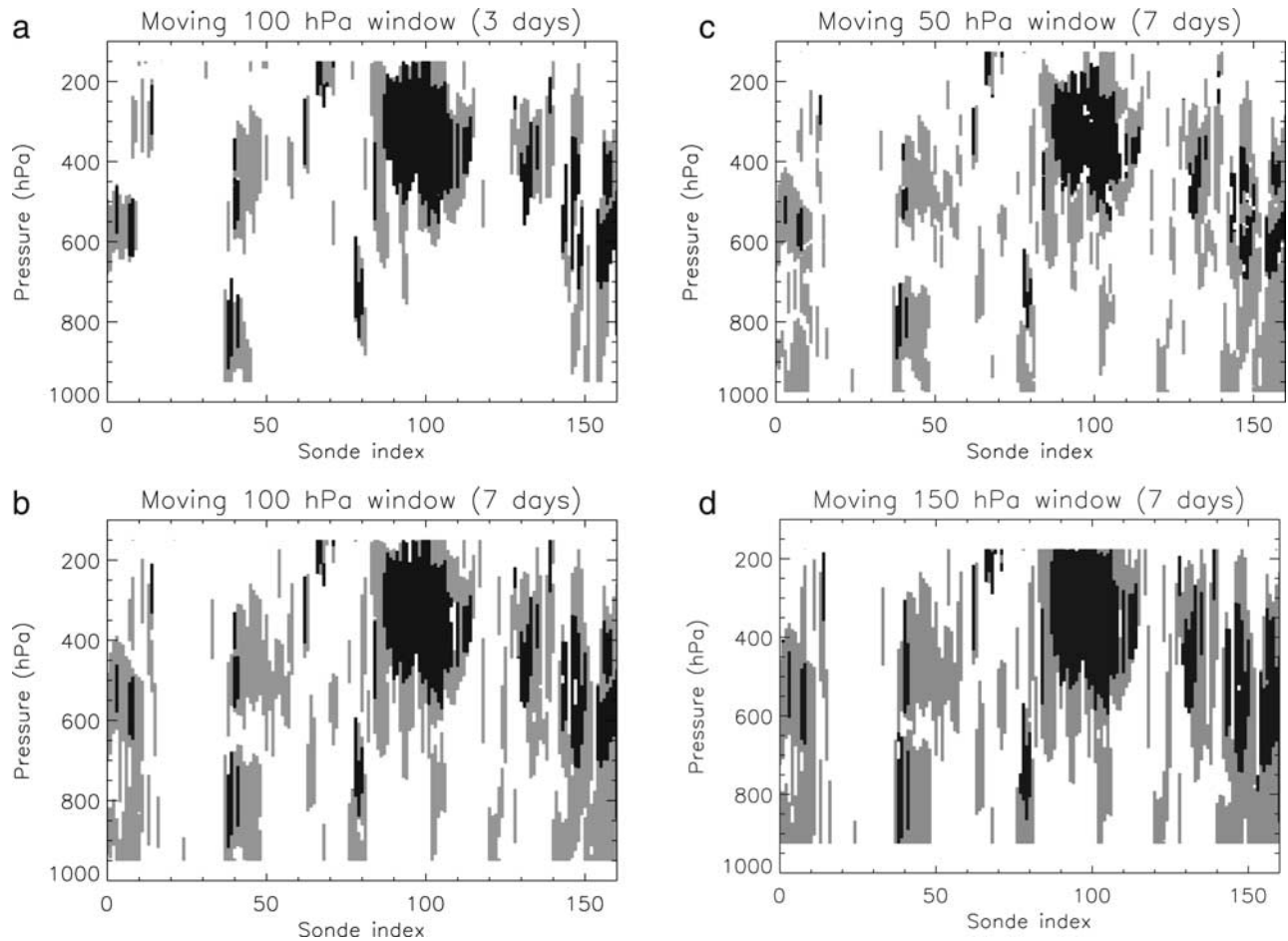


Figure 11. Occurrence of dry layers predicted by the model and comparison with radiosonde data. The x-axis shows the sonde index corresponding to November–December 1992 (see Figure 8), and the y-axis shows the pressure at which dry intrusions are predicted/seen. A window of given width is centered at each pressure level, and if the model predicts dry air anywhere within this window, that point has a grey color. If the sonde also observes a dry layer anywhere within the same window, that point has a black color. Dry intrusions are defined as air masses with RH lower than 20%. (a) and (b) Correspond to trajectories of 3 and 7 days and a window of 100 hPa. (c) and (d) Obtained with trajectories of 7 days but using a window of 50 hPa (Figure 11c) and 150 hPa (Figure 11d).

has experienced ascent. It is clear that most of the dry events in Figure 11 are associated with air that has descended. However in the boundary layer moistening of air eliminates most dry anomalies. This interpretation is confirmed by the change in specific humidity associated with processes other than condensation, shown in Figure 12c. There is an increase in specific humidity below 850 hPa wherever the trajectory model predicts a dry intrusion (Figure 11b). In other words, while q_{traj} implies a low RH there, the analysis shows a much higher value of specific humidity, $q(t_0)$.

[35] Figure 12b shows the latitude of the origin of 7-day trajectories. Most air is tropical in origin but some significant dry events are associated with extratropical air. These include the events in the lower troposphere around sonde indices 5 and 40, associated with intrusions from the Southern Hemisphere, and those associated with air from the Southern Hemisphere occurring at sonde indices 80, 120–125 and 140–160.

[36] Figure 13 shows the condensation occurring along each 7-day trajectory as inferred from the difference between the analyzed specific humidity at the origin of the

trajectory, $q(t_0 - 7)$, and the specific humidity assigned to the trajectory, q_{traj} (see section 2 and Figure 1). A direct comparison between Figures 12a and 13 shows that most condensation is associated with significant vertical ascent (blue in Figure 12a), most likely associated with regions of deep convection in the analysis model. None of the dry events in Figure 11 are associated with condensation over the last week.

6.2. Selected Dry Events

[37] In this section, 12-day back trajectories will be examined for four dry events. In each case there is agreement between the trajectories and radiosondes as shown by black points in Figure 11. Two of those events are in the upper troposphere (around sondes 60 and 100) and two in the lower troposphere (around sondes 40 and 80). They are referred to as clusters 1–4, respectively, in Figure 14.

[38] Cluster 1 corresponds to a single vertical profile in Figure 11 at sonde 61 (20 November 1992, 5:00am). The colors in the plot go from blue - red - yellow, corresponding to a regular sampling of this profile, moving upward.

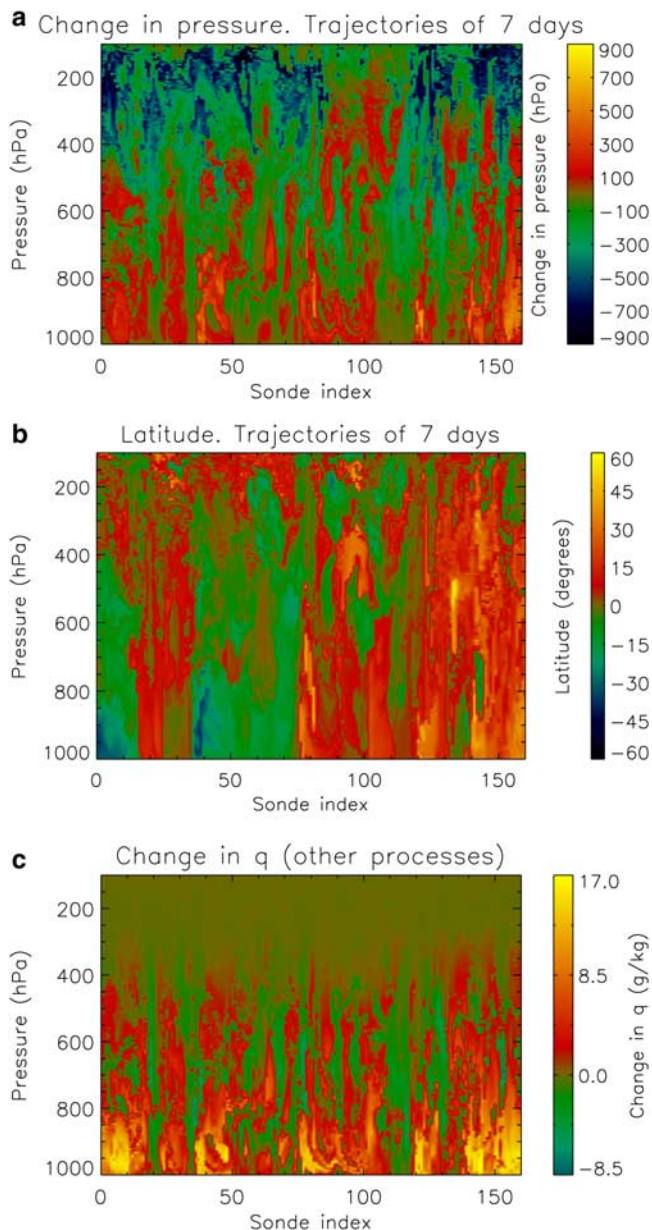


Figure 12. Changes in pressure (top) experienced along the trajectory, and latitude (middle) of the origin of air masses arriving at Kapingamarangi during November–December 1992. Trajectories of 7 days are used. The plot at the bottom shows the diagnosed changes in specific humidity q (g/kg) since last condensation occurred ($q(t_0) - q_{traj}$) or from 7 days ago if no condensation occurred (so that $q_{traj} = q(t_0 - 7)$).

[39] The trajectories show three major contributions. One is air advected from the lower troposphere in the Southern Equatorial Indian Ocean. The other two are upper tropospheric branches from the Northern and Southern Hemispheres. This situation is not associated with significant changes in potential vorticity, and the inertial instability of the air is suggested by the trajectories from 0° – 40° E.

[40] Cluster 2 shows trajectories corresponding to the prolonged dry period in the upper troposphere around sonde 100 (2–8 December) in Figure 11. To select the trajectories

plotted in the figure, each of the sondes was sampled regularly in the vertical and each sonde was sampled one after the other. At the beginning (blue trajectories) the contribution is from both hemispheres, then air mainly originates from the Northern Hemisphere (green, red), and finally it is dominated by air which is almost stationary (yellow). Over the last 7 days before arrival all of these trajectories are found close to Kapingamarangi, indicating a stagnant region of dry air.

[41] Cluster 3 shows trajectories corresponding to the lower tropospheric event around sonde 40 (12–13 November). Figure 12 already suggests that most of it is associated with descending air from the Southern Extratropics, and this is shown in more detail in Figure 14. This event was previously studied by *Mapes and Zuidema* [1996] and also by *Yoneyama and Parsons* [1999], whose Figure 7 directly compares with our figure (only one trajectory is shown by them, indicated with crosses). The trajectories are consistent, even though they used a different data set, the global analysis (GANAL) from the Meteorological Agency of Japan.

[42] Cluster 4 was associated with strong descent (over 7 days) in Figure 12a near sonde 80 (26 November). The clusters of green, red and yellow trajectories correspond to different times during this dry event. The trajectories mostly start in the subtropics and typically ascend as they move polewards. Then they curve anticyclonically and descend into the tropics. This dry event was also studied by *Yoneyama and Parsons* [1999] and is shown in their Figure 7 by a single trajectory denoted by stars.

[43] Note that the trajectory origins indicate a flip from Southern Hemisphere to Northern Hemisphere beginning on 24 November (sonde index 76) in the lower troposphere (Figure 12b). More work is needed to investigate whether this may be a rapid local manifestation of the seasonal transition between Southern and Northern Hemisphere Hadley cells.

7. Conclusion

[44] The origin of dry intrusions observed by radiosonde profiles in the tropical West Pacific has been investigated using winds and humidity from ERA-40. The work has

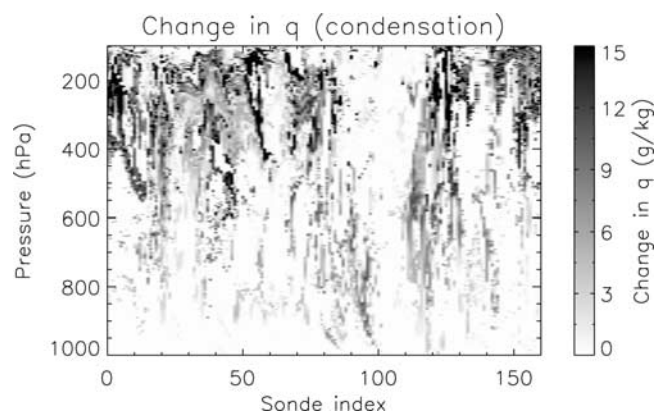


Figure 13. Diagnosed increase in specific humidity q (g/kg) due to condensation ($q(t_0 - 7) - q_{traj}$) along 7 day trajectories arriving above Kapingamarangi in November–December 1992.

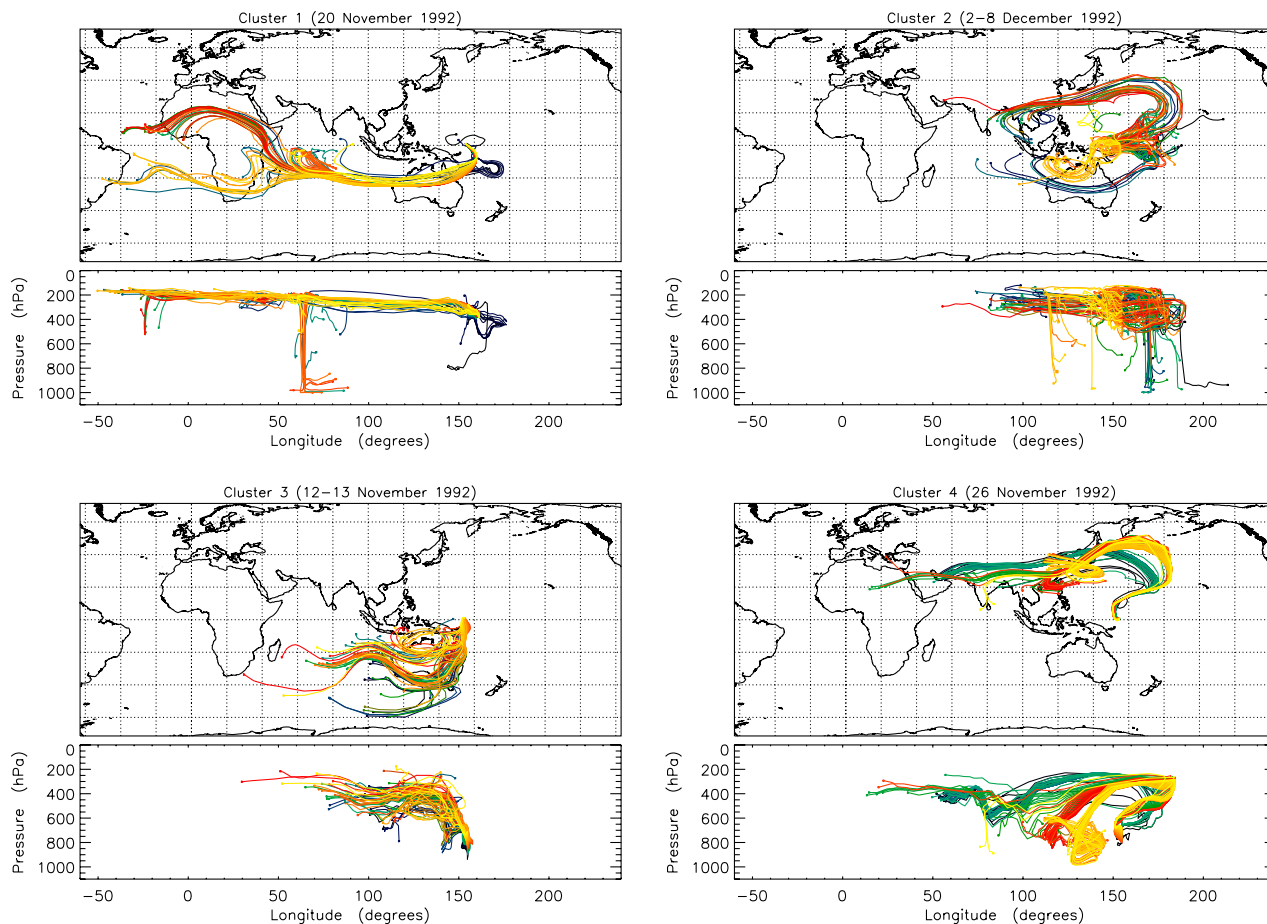


Figure 14. Twelve-day back trajectories for four dry events at Kapingamarangi (154°E , 01°N). With reference to Figure 11 they correspond to the dry events (black) in the upper troposphere on 20 November 1992 (cluster 1 - sonde 61), the first decad of December (cluster 2, around sonde 100), in the lower troposphere on 12–13 November (cluster 3, around sonde 40), and 26 November (cluster 4, around sonde 80). The trajectories shown are a regular sample of the many associated with the dry events. See text for an explanation of the coloring.

concentrated on dry intrusions which have a significant impact on radiative transfer. It is shown that the increase in OLR due to dry intrusions in a clear sky scenario scales almost linearly with their vertical extent (typically 3 Wm^{-2} per 100 hPa thickness) and varies little with their altitude. The presence of clouds reduces the radiative impact of a dry intrusion, even if the cloud deck is below the intrusion. A study of the heating rates associated with four dry intrusions, all with a vertical extent of 100 hPa or more, has shown that they reduce cooling from the level of the intrusion but increase it just below, tending to create a temperature inversion at the lower edge. Although the layer between the dry intrusion and the ground may be destabilized by cooling the top of this layer, the strengthening of the capping inversion, together with the dryness of the intrusion, could inhibit convection penetrating from below, helping to maintain the intrusion [Mapes and Zuidema, 1996].

[45] Focusing attention on these dry intrusions, ERA-40 fields have been used to reconstruct the relative humidity profiles observed by the radiosondes by conserving specific humidity along trajectories but accounting for condensation if saturation occurs. It is found that the two profiles agree

well, although the reconstructed profiles correlate best with sondes for short trajectories. Beyond trajectory lengths of one day the anomaly correlations reduce only slowly with time, indicating that the air mass origins are consistent with dry air over very long trajectories. This approach was then extended, matching the occurrence of dry intrusions in both the observed and the reconstructed RH profiles, allowing for small displacement errors in the dry intrusions by comparing the two over moving windows. It was found that with this approach all intrusions observed by the radiosondes were also predicted by the model. Given this good agreement, the trajectories of the dry air masses were used to investigate their origin. A variety of behaviors was found, with many dry events clearly associated with air masses descending from the extratropics. The changes in specific humidity along trajectories, partitioning condensation from all other processes, also give a useful indication of air mass history and water vapor transport.

[46] Given the successful validation of using back trajectories based on ERA-40 data to diagnose the origin of tropical dry layers at one station, this technique is now being used to examine the origin of dry air in the whole tropical region.

[47] **Acknowledgments.** We are grateful to Keith Shine for stimulating discussions on radiative transfer and for providing the software developed by him and his collaborators. We are also grateful to Maarten Ambaum, who drew our attention to SG filters and Sergio Pezzulli for stimulating discussion on bootstrap techniques. Piero Cau is funded by the Natural Environment Research Council grant NER/T/S/2001/00195 as part of their Clouds, Water Vapour and Climate thematic programme. John Methven is grateful for an Advanced Fellowship sponsored jointly by the Natural Environment Research Council and the Environment Agency.

References

- Ciesielski, P., and R. Johnson (2003), Corrected TOGA COARE sounding humidity data: Impact on diagnosed properties of convection and climate over the warm pool, *J. Clim.*, *16*, 2370–2384.
- Gibson, J., P. Källberg, S. Uppala, A. Nomura, A. Hernandez, and E. Serrano (1997), ERA description, *ECMWF Re-Anal. Proj. Rep. Ser.*, *1*.
- Mapes, B., and P. Zuidema (1996), Radiative-dynamical consequences of dry tongues in the tropical troposphere, *J. Atmos. Sci.*, *53*, 620–638.
- Methven, J. (1997), Offline trajectories: Calculation and accuracy, *Tech. Rep. 44*, U.K. Univ. Global Atmos. Modell. Programme, Dep. of Meteorol., Univ. of Reading, Reading, U.K.
- Methven, J., S. Arnold, F. O'Connor, H. Barjat, K. Dewey, J. Kent, and N. Brough (2003), Estimating photochemically produced ozone throughout a domain using flight data and a Lagrangian model, *J. Geophys. Res.*, *108*(D9), 4271, doi:10.1029/2002JD002955.
- Mudelsee, M. (2003), Estimating Pearson's correlation coefficient with bootstrap confidence interval from serially dependent time series, *Math. Geol.*, *35*(6), 651–665.
- Namias, J. (1936), Structure and maintenance of dry-type moisture discontinuities not developed by subsidence, *Mon. Weather Rev.*, *64*, 351–358.
- Nordquist, W. (1973), Numerical approximations of selected meteorological parameters for cloud physics problems, *Tech. Rep. ECOM-5475*, Atmos. Sci. Lab., U.S. Army Electron. Command, White Sands Missile Range, N. M.
- Pierrehumbert, R. (1995), Thermostats, radiator fins, and the local runaway greenhouse, *J. Atmos. Sci.*, *52*, 1784–1806.
- Politis, N., and J. Romano (1994), The stationary bootstrap, *J. Am. Stat. Assoc.*, *89*(428), 1303–1313.
- Press, W., B. Flannery, S. Teukolsky, and W. Vetterling (1992), *Numerical Recipes: The Art of Scientific Computing*, 702 pp., Cambridge Univ. Press, New York.
- Shine, K. P. (1991), On the cause of the relative greenhouse strength of gases such as the halocarbons, *J. Atmos. Sci.*, *48*, 1513–1518.
- Shine, K. P., and A. Sinha (1991), Sensitivity of the Earth's climate to height-dependent changes in the water vapour mixing ratio, *Nature*, *354*, 382–384.
- Simmons, A. (2001), Development of ERA-40 data assimilation system, *ERA-40 Proj. Rep. Ser.*, *3*, 11–30.
- Simmons, A., and J. Gibson (2000), The ERA-40 Project Plan, *ERA-40 Proj. Rep. Ser.*, *1*.
- Simmons, A., A. Untch, C. Jakob, P. Kallberg, and P. Unden (1999), Stratospheric water vapour and tropical tropopause temperatures in ECMWF analyses and multi-year simulations, *Q. J. R. Meteorol. Soc.*, *125*, 353–386.
- Stohl, A. (1998), Computation, accuracy and applications of trajectories—A review and bibliography, *Atmos. Environ.*, *32*, 947–966.
- Wang, J., H. Cole, D. Carlson, E. Miller, K. Beierle, A. Paukkunen, and T. Laine (2002), Corrections of humidity measurement errors from the Vaisala RS80 radiosonde - Application to TOGA COARE data, *J. Atmos. Oceanic Technol.*, *19*, 981–1002.
- Webster, P., and R. Lukas (1992), TOGA-COARE: The coupled ocean-atmosphere response experiment, *Bull. Am. Meteorol. Soc.*, *73*, 1377–1416.
- Yoneyama, K., and D. Parsons (1999), A proposed mechanism for the intrusion of dry air into the tropical western Pacific region, *J. Atmos. Sci.*, *56*, 1524–1546.

P. Cau, B. Hoskins, and J. Methven, Department of Meteorology, University of Reading, P.O. Box 243, Earley Gate, Reading RG6 6BB, UK. (p.cau@reading.ac.uk)